Springer

KSME

Journal of Mechanical Science and Technology 24 (8) (2010) 1583~1594
www.springerlink.com/content/1738-494x
DOI 10.1007/s12206-010-0507-0

# Correlation study of a rotor in descending flight using DYMORE with a freewake model †

Jae-Sang Park, Sung Nam Jung*, Soo Hyung Park and Yung Hoon Yu

*Department of Aerospace Information Engineering, Konkuk University, Seoul, 143-701, Korea*

(Manuscript Received July 1, 2009; Revised February 1, 2010; Accepted April 14, 2010)

**Abstract**

In this work, the Blade Vortex Interaction (BVI) airloads characteristic for a rotor in descending flight condition is investigated using a nonlinear flexible multibody dynamics analysis code DYMORE. A free vortex wake model is incorporated into the comprehensive analysis system and improvement of airloads prediction as well as collective and cyclic pitch control settings is obtained over the finite-state dynamic inflow model that is adopted in the conventional DYMORE analysis. The three test conditions in the HART (Higher harmonic control Aeroacoustic Rotor Test) II are considered to illustrate the present investigation. It is found that the BVI airloads characteristic is significantly influenced by the higher harmonic pitch control inputs. The influence of BVI oscillatory peaks along with the miss-distance between the blade and the vortices is studied in detail to identify the mechanism of reducing noise and vibration in the HART II experiment.

*Keywords*: Freewake; HART II; Multibody analysis; Rotor

## 1. Introduction

The Blade Vortex Interaction (BVI) of rotorcrafts is caused by interaction between the rotor blades and wakes. BVI occurs mainly during low speed descending flight and causes significant noise and vibration for rotorcrafts. In a means to improve the basic understanding and the prediction capabilities of BVI phenomena, the international joint programs – Higher harmonic control Aeroacoustic Rotor Test (HART) I [1] and II [2] - were conducted in 1994 and 2001, respectively, by researchers from German DLR, French ONEAR, US NASA Langley, US Army (AFDD) and Netherlands DNW. Particularly, the goals of the programs are to measure and predict comprehensive acoustics, rotor wakes, aerodynamics, and blade deformations of the rotor with and without higher harmonic pitch control (HHC) inputs. For both HART I and II, 40% Mach and dynamically scaled models of the BO-105 hingeless rotors in the open-jet anechoic test section of the German-Dutch Wind tunnel (DNW) were used (Fig. 1). With wind tunnel tests, each participating organization conducted the prediction analysis using their own rotor comprehensive analysis codes such as HOST [3], CAMRAD-II and S4 [4].

Although the rotor comprehensive analysis with the multiple trailer wake model gives better predictions of the sectional lift variation of the HART I/II than the analysis with the rollup wake model does [4, 5], there are still discrepancies between predictions from comprehensive analysis and the experimental results. During the last decade, in order to predict BVI airloads more accurately, Comprehensive Structural Dynamics (CSD)/Computational Fluid Dynamics (CFD) coupled analyses for the HART I/II have been studied [6-9]. The loose coupling analyses based on a trimmed, periodic rotor solution predict BVI airloads well and reduce the discrepancy between the numerical and experimental results, as compared with the results of CSD analysis alone. However CSD/CFD coupled analysis requires huge computing resources.

Recently, flexible multibody dynamics modeling based on topology and its analysis have been applied to rotorcrafts [10-13]. DYMORE is a nonlinear flexible multibody dynamics analysis code that has been developed by Bauchau [14]. DYMORE is able to construct a multibody modeling using rigid/elastic joints, rigid bodies, and elastic bodies such as beams, plates, and shells. This powerful multibody modeling capability of DYMORE is very effective at representing complicated rotor systems elaborately, although DYMORE has not been specially developed for rotor comprehensive analysis. DYMORE uses geometrically exact beam theory [15] for nonlinear elastic beam modeling and the finite-state dynamic inflow model [16] for the aerodynamic modeling of the blade. However, since the finite-state dynamic inflow model in

† This paper was recommended for publication in revised form by Associate Editor Yeon June Kang

* Corresponding author. Tel.: +82 2 450 3449, Fax: +82 2 444 6106
E-mail address: snjung@konkuk.ac.kr

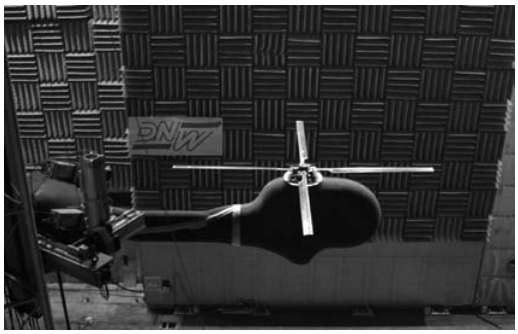


Fig. 1. HART II rotor in DNW wind tunnel.

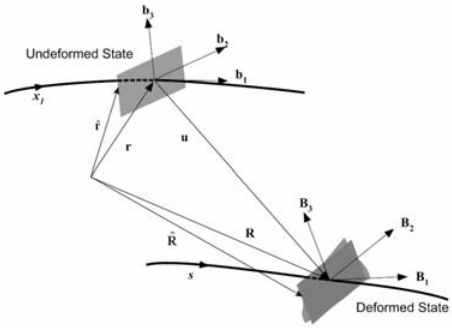


Fig. 2. Deformed and undeformed states of the beam [15].

DYMORE is relatively too simple to predict the complex aerodynamic environment of rotorcrafts, DYMORE should be coupled with the external CFD codes in order to predict the blade airloads well [9, 17].

To improve the rotor wake modeling capability of DYMORE, Roget [11] focused to incorporate the Bhagwat-Leishman (B-L) freewake model [18] into DYMORE. However, numerical results on the vibratory loads analysis for Active Twist Rotor (ATR) and Active Trailing-edge Flap (ATF) blades showed large differences in vibratory load magnitudes between the prediction and the experiment.

So far, no published effort has been made to analyze BVI airloads of a rotor in descending flight using a nonlinear flexible multibody dynamics analysis code DYMORE, especially with the free vortex wake model. In the present work, the prediction capability of DYMORE is assessed using the free wake method developed by B-L [18] and later by Roget [11] for the estimation of BVI airloads of the HART II rotor, with and without the higher harmonic pitch control (HHC) inputs. The BVI airload characteristic coupled with miss-distance between the blade and the vortices is investigated to understand the mechanism behind the reduction of noise and vibration levels of the various test cases conduced in the HART II. There is no opposition that more refined analysis such as a CSD/CFD coupled analysis is truly needed to identify BVI phenomenon thoroughly, however, a simple and efficient but reasonably reliable comprehensive analysis system is equally desirable for preliminary results and also for acquiring physical insights about the complex fluid-structure interaction phenomena. In this regard, the present approach deserves to be performed and will serve as a stepping stone toward more sophisticated methods.

## 2. Formulations for rotor aeroelastic analysis

In this section, a nonlinear elastic beam theory in DYMORE for the blade structural dynamics and a freewake model that is incorporated in DYMORE for the aerodynamics on the blade for the present work are described briefly.

### *2.1 Geometrically exact beam theory*

The geometrically exact beam theory [15] for nonlinear elastic beams is employed in DYMORE. In order to apply this beam theory effectively to the flexible multibody dynamic system with arbitrary topology, DYMORE, there are two slight modifications from the original formulation. One is that the reference coordinate is a single inertial Cartesian coordinate instead of a moving and deformed coordinate. The other is that the displacement-based formulation is used instead of the mixed formulation.

Fig. 2 shows the coordinates between the undeformed and deformed states of the beam. The beam is idealized as a reference line and a typical reference cross-section. Let $x_1$ denote arc-length along a curved reference line within an undeformed, initially curved and twisted beam. At each point along the reference line in the undeformed configuration, an orthonormal triad $\mathbf{b}_i$ is introduced such that $\mathbf{b}_i$ is tangent to $x_i$. Latin indices assume 1, 2, and 3 in this paper. $\mathbf{B}_i$ is another orthonormal triad defined in the deformed configuration, which has the following relationship with an orthonormal triad $\mathbf{b}_i$ in the undeformed state as

$$\mathbf{B}_i = \mathbf{C}^{Bb} \bullet \mathbf{b}_i = C_{ij}^{Bb}\mathbf{b}_j \tag{1}$$

where $\mathbf{C}^{Bb} = C_{ij}^{Bb}\mathbf{b}_i\mathbf{b}_j$ denotes the rotation tensor which has nine elements and is represented by Wiener-Milenkovic parameters [19]. In addition, $\mathbf{u} = u_i\mathbf{b}_i$ is the displacement vector including the rigid body motion and elastic deformation of the reference line from the reference configuration and $\mathbf{r}$ is the position vector of the points of the reference line in the undeformed state.

The equation of motion for the geometrically exact beam theory with displacement-based formulation is derived from Hamilton's principle as

$$\int_{t_1}^{t_2}\int_0^L \left[\delta\mathbf{V}^T\mathbf{P} + \delta\boldsymbol{\Omega}^T\mathbf{H} - \delta\boldsymbol{\gamma}^T\mathbf{F} - \delta\boldsymbol{\kappa}^T\mathbf{M} + \overline{\delta\mathbf{q}}^T\mathbf{f} + \overline{\delta\boldsymbol{\psi}}^T\mathbf{m}\right]dx_1 dt = 0 \tag{2}$$

where $t_1$ and $t_2$ are arbitrary fixed times, $L$ is the length of the beam. $\mathbf{P}$ and $\mathbf{H}$ are the linear and angular momentum vectors, and $\mathbf{F}$ and $\mathbf{M}$ are the internal forces and moment vectors. These four quantities are defined in the $\mathbf{B}_i$ coordinate and obtained from the constitutive relationship. $\overline{\delta\mathbf{q}}$ and $\overline{\delta\boldsymbol{\psi}}$ are the virtual displacements and the virtual

rotations which are the counterparts to the distributed applied forces and moments per unit length $\mathbf{f}$ and $\mathbf{m}$, respectively. Note that the bars over variations are used to indicate that the virtual quantities need not be the variations of function or functionals. $\boldsymbol{\gamma}$ and $\boldsymbol{\kappa}$ denote the force strain vector and the curvature strain vector, and $\mathbf{V}$ and $\boldsymbol{\Omega}$ are the linear velocity vector and the angular velocity vector. Their variations are given as follows

$$\delta\boldsymbol{\gamma} = \mathbf{C}^{BI}\left[\left(\tilde{\mathbf{r}}_I' + \tilde{\mathbf{u}}_I'\right)\overline{\delta\boldsymbol{\psi}}_I + \delta\mathbf{u}_I'\right] \tag{3}$$

$$\delta\boldsymbol{\kappa} = \mathbf{C}^{BI}\overline{\delta\boldsymbol{\psi}}_I' \tag{4}$$

$$\delta\mathbf{V} = \mathbf{C}^{BI}\left(\dot{\tilde{\mathbf{u}}}_I\overline{\delta\boldsymbol{\psi}}_I + \delta\dot{\mathbf{u}}_I\right) \tag{5}$$

$$\delta\boldsymbol{\Omega} = \mathbf{C}^{BI}\dot{\overline{\delta\boldsymbol{\psi}}}_I \tag{6}$$

where the notation $\widetilde{(\,)}$ forms an antisymmetric matrix from a vector according to $\widetilde{(\,)}_{ij} = -e_{ijk}(\,)_k$ with the permutation symbol $e_{ijk}$ and the subscript $I$ implies the inertial frame. In addition, the superscripts with prime and dot in this section denote the derivatives with respect to $x_1$ and time, respectively.

Eq. (2) can be discretized appropriately for the finite element method with up to 3rd-order interpolation polynomials in DYMORE. As one can see, the equation of motion is formulated in Cartesian inertial coordinates and it is limited to small strains.

### *2.2 Aerodynamic model with freewake*

A two-dimensional airfoil theory with an airfoil table look-up is used to obtain the aerodynamic forces and moments acting on the blade. For an inflow model, Peters and He's finite-state dynamic inflow model [16] is used originally in DYMORE. This model is constructed by applying the acceleration potential theory to a rotor aerodynamics problem with a skewed cylindrical wake. More specifically, the induced flow at the rotor disk was expanded in terms of modal functions. As a result, a three-dimensional, unsteady induced-flow aerodynamics model with a finite number of states is derived in time domain. This model is an intermediate level of wake representation between the simplest momentum and the most complicated freewake methodologies. Detailed explanation for the finite-state dynamic inflow model is given in the reference [16]. However, this finite-state dynamic inflow model is not capable of capturing rotor wakes well in low speed forward flight of helicopters. Therefore, based on the previous research [11], the freewake model [18] is implemented in DYMORE in order to predict BVI airloads of the HART II more accurately. This section briefly describes the formulation for the freewake model.

The freewake analysis is based on a potential flow with the vorticity assumed to be concentrated on a finite number of vortex filaments. The motion of a point on a vortex filament as depicted in Fig. 3 is described by the motion of Lagrangian

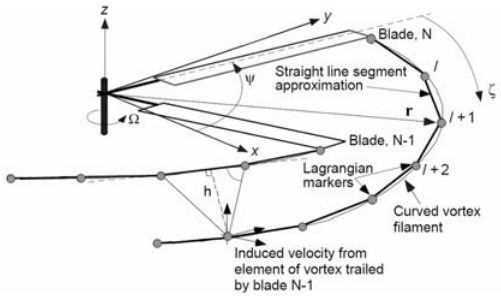


Fig. 3. Lagrangian description of the vortex filaments trailing from the blade tips [18].

fluid markers as

$$\frac{d\mathbf{r}(\psi,\zeta)}{dt} = \mathbf{V}\left(\mathbf{r}(\psi,\zeta)\right) \tag{7}$$

where $\mathbf{r}$ is the position vector of the point on the vortex filament and $\mathbf{V}$ is the local fluid velocity at the point $\mathbf{r}$. In addition $\psi$ and $\zeta$ denote the blade azimuth angle and wake age, respectively. From Eq. (7), the vorticity transport equation can be expressed in the following partial differential form as

$$\frac{d\mathbf{r}(\psi,\zeta)}{d\psi} + \frac{d\mathbf{r}(\psi,\zeta)}{d\zeta} = \frac{\mathbf{V}\left(\mathbf{r}(\psi,\zeta)\right)}{\Omega} \tag{8}$$

where $\Omega$ is the rotational velocity of a rotor. Eq. (8) is the governing equation for the free-vortex problem applied to the rotor wake. The velocity $\mathbf{V}$ at a marker consists of the free stream velocity $\mathbf{V}_\infty$, induced velocity $\mathbf{V}_{\text{ind}}$ and general external velocity $\mathbf{V}_{\text{ext}}$.

The induced velocity $\mathbf{V}_{\text{ind}}$ which is highly nonlinear is calculated from the Biot-Savart law:

$$\mathbf{V}_{\text{ind}}(r) = \frac{\Gamma}{4\pi}\frac{h^2}{\sqrt{h^2 + r_c^2}}\int\frac{d\mathbf{l}\times d\mathbf{r}}{|\mathbf{r}|^3} \tag{9}$$

where $\Gamma$ is the circulation strength of the vortex segment, $h$ is the perpendicular distance of the evaluation point from the influencing vortex element (Fig. 3), and $d\mathbf{l}$ is the vortex segment. The core radius $r_c$ is given as

$$r_c(\zeta) = \sqrt{r_{\text{initial}}^2 + 4\alpha\delta\nu\zeta/\Omega} \tag{10}$$

where $\alpha$ is an empirical factor with the value of 1.25643, $\delta$ is the apparent viscosity coefficient, and $\nu$ is the kinematic viscosity.

The domain $(\psi, \zeta)$ is discretized into finite steps of $\Delta\psi$ and $\Delta\zeta$ to solve Eq. (8) numerically. In addition, the derivatives on the left-hand-side of Eq. (8) can be approximated by the finite difference approximation with the 2nd-order accurate, five-point central difference scheme. The discretized equation is integrated by applying the time marching algo-

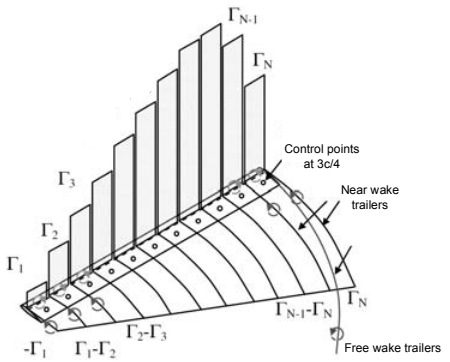


Fig. 4. Geometry of near wakes [11].

rithm using predictor-corrector with the 2nd-order backward difference (PC2B) proposed by Bhagwat and Leishman [18] and modified by Roget [11]. The detailed expressions for PC2B can be obtained from references [11, 18].

The trailed near wake is also considered with the freewake to improve the accuracy of rotor wakes. The near wake consists of a series of vortex filaments trailed behind the blade for a given distance, typically 30°, as seen in Fig. 4. Therefore the velocity at the control point located at the 3/4 chord location depends on the influence of four components; the free stream, the far wake, the near wake, and the bound vortex. The boundary condition that the component of the velocity normal to the panel must be zero at the control point is applied to solve the blade bound vorticity problem.

Given the theories described above, the airfoil tables with C-81 format are used as follows. First, the aerodynamic lift is estimated by the two-dimensional strip theory using the inflow distribution obtained from the freewake. Second, from the estimated lift, the angle of attack for the equivalent flat plate is determined. Third, the surface normal vector at the control point is adjusted to make it consistent with the equivalent flat plate angle of attack. Fourth, the blade bound circulations and the equivalent lifts are calculated. Finally, the effective angle of attack at each air station point is determined from a reverse table look-up procedure. This procedure allows for the circulation distribution on the blade to be consistent with the circulation released into the freewake.

## 3. Numerical results

This section describes the correlation results between the DYMORE predictions and measurement data for the HART II, with and without HHC inputs. Through this correlation study, the capability of DYMORE with a freewake model to predict BVI airloads is investigated. These include rotating natural frequencies, pitch control settings, BVI airloads, and blade deformations for the three test cases considered in the HART II [22].

### *3.1 Modeling of the HART II rotor*

As mentioned previously, the HART II rotor is a 40% geometrically and dynamically scaled model of the full-scale hingeless BO105 main rotor. The rotor was scaled to match the natural frequencies in 1st and 2nd flap (1F and 2F), 1st lead-lag (1L), and 1st torsion (1T) at 100% RPM in terms of n/rev (*n*P) with the full-scale rotor. The general properties of the rotor are summarized in Table 1. The details of the blade structural properties are given in the HART II technical document [20].

Table 1. General properties of the HART II rotor blade [20].

| | |
|---|---|
| Rotor type | Hingeless |
| Scale type | Mach |
| Planform | Rectangular |
| Number of blades, $N$ | 4 |
| Radius, $R$ | 2.0 m |
| Radius pitch bearing | 0.075 m |
| Root cutout | 0.44 m |
| Radius zero twist | 1.5 m |
| Chord length, $c$ | 0.121 m |
| Solidity, $\sigma$ | 0.077 |
| Pitch arm | 0.063 m |
| Airfoil | NACA23012mod |
| Tab length | 0.0054 m |
| Tab thickness | 0.0008 m |
| Linear twist | -8.0 deg. |
| Precone angle | 2.5 deg. |
| Blade mass | 2.24 kg |
| Lock number | 8.06 |
| Nominal rotor speed, $\Omega_{ref}$ | 109.0 rad/s |

Although DYMORE is capable of constructing a multibody modeling including complicated rotor control systems such as pitch links, pitch horns, and rotating/nonrotating swashplates, since there is no available information about detailed geometric, stiffness, and inertial properties of the rotor control system components of the HART II, four nonlinear elastic blades and a rigid hub are used for the present DYMORE modeling, as shown in Fig. 5. For the finite element modeling, a rotor blade is discretized into 10 beam elements with 3rd order interpolation polynomials. Since it is a hingeless rotor, there is only a feathering hinge that is modeled as a revolute joint. In the present modeling, to match the 1st torsional frequency at the nominal rotor speed, a torsional spring with appropriate value describing the rotor control system stiffness is used at the feathering hinge joint. The hub is modeled as a rigid body, and is connected with a revolute joint at a prescribed rotational speed. Although this work uses a relatively simple multibody modeling, an elaborate multibody modeling including various rotor control system components will be introduced for the next HART III program [21] in the near future. For aerodynamic loads on the blade, total 31 air station points with an equal spacing are used, and the value of 10% chord length is used for the initial core radius $r_{initial}$ at the tip in the free wake modeling.

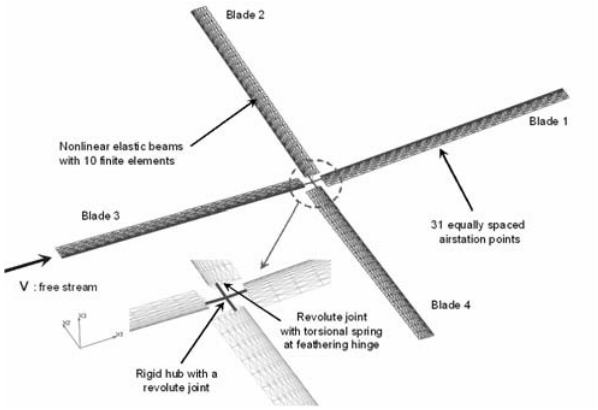


Fig. 5. DYMORE modeling for the HART II rotor.

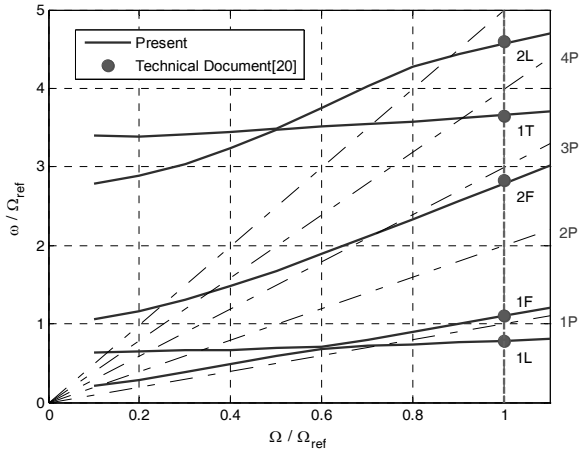


Fig. 6. Fan plot analysis result of HART II rotor blade.

### *3.2 Fan plot analysis*

To validate the structural dynamics modeling of the HART II rotor, the fan plot analysis is conducted as given in Fig. 6. Five natural frequencies including the first and second flaps, first and second lead-lags, and first torsion are predicted as the rotating speed is increased. The natural frequencies and rotating speed are non-dimensionalized by the rotor nominal speed, 109.0 rad/s. As one can see, the predicted natural frequencies have excellent agreement with the results from the HART II technical document [20]. Particularly, the 1st torsional frequency prediction is the most important in structural dynamics modeling since the torsional behavior of the rotor blade is closely related to the lift variation.

### *3.3 Trim analysis*

There are three test cases for the HART II. The baseline (BL) case is for the test without HHC inputs. The others are for the minimum noise (MN) and minimum vibration (MV) test cases with appropriate 3/rev HHC inputs. The test conditions for the BL, MN, and MV are given in Table 2 [22]. Note that the positive direction for the thrust is upward and the positive directions for the rolling and pitching moments are advancing side down and nose up, respectively. In addition, $\theta_{3c}$ and $\theta_{3s}$ are the cosine and sine components of 3/rev HHC inputs, respectively. Before BVI airload predictions are discussed, the trim analysis results for three test cases are investigated. For the rotor trim with given flight conditions, an autopilot theory is used to match the desired trim target values of

Table 2. HART II test conditions [22].

| | |
|---|---|
| Tip Mach number, M | 0.6387 |
| Advance ratio, $\mu$ | 0.15 |
| Shaft tilt angle*, $\alpha_s$ | 4.5 deg. |
| • Baseline (BL) case | |
| Thrust | 3300 N |
| Rolling moment | 20 N-m |
| Pitching moment | -20 N-m |
| • Minimum Noise (MN) case | |
| Thrust | 3300 N |
| Rolling moment | 30 N-m |
| Pitching moment | -30 N-m |
| $\theta_{3c}$ (HHC lateral cyclic pitch angle) | 0.41 deg. |
| $\theta_{3s}$ (HHC longitudinal cyclic pitch angle) | -0.70 deg. |
| • Minimum Vibration (MV) case | |
| Thrust | 3290 N |
| Rolling moment | 20 N-m |
| Pitching moment | -30 N-m |
| $\theta_{3c}$ (HHC lateral cyclic pitch angle) | -0.79 deg. |
| $\theta_{3s}$ (HHC longitudinal cyclic pitch angle) | 0.00 deg. |

* : Effective shaft tilt angle considering wind tunnel interference.

Table 3. Trim analyses results.
(a) BaseLine (BL) case

| | Experiment | Dymore | |
|---|---|---|---|
| | | Freewake | Finite-state dynamic inflow |
| $\theta_0$ | 3.2° | 3.690° | 4.011° |
| $\theta_{1c}$ | 2.0° | 2.055° | 1.365° |
| $\theta_{1s}$ | -1.1° | -1.113° | -1.398° |

(b) Minimum Noise (MN) case

| | Experiment | Dymore | |
|---|---|---|---|
| | | Freewake | Finite-state dynamic inflow |
| $\theta_0$ | 3.15° | 3.714° | 4.010° |
| $\theta_{1c}$ | 2.04° | 2.051° | 1.323° |
| $\theta_{1s}$ | -1.07° | -1.197° | -1.482° |

(c) Minimum Vibration (MV) case

| | Experiment | Dymore | |
|---|---|---|---|
| | | Freewake | Finite-state dynamic inflow |
| $\theta_0$ | 3.16° | 3.714° | 4.001° |
| $\theta_{1c}$ | 2.04° | 2.102° | 1.376° |
| $\theta_{1s}$ | -1.11° | -1.168° | -1.449° |

thrust, pitch, and rolling moments given in Table 2.

Table 3 shows the results of trim analyses for the BL, MN, and MV cases. Two wake/inflow models such as freewake and finite-state dynamic inflow models are used and the results are compared with the experimental results [3]. As is seen, both trim analyses using freewake and finite-state dynamic inflow models over-predict the collective pitch angle $\theta_0$ of all three test cases as compared with the wind tunnel test results. However, the result with a freewake model shows better correlation than that with the finite-state dynamic inflow model. For the two cyclic pitch angles $\theta_{1c}$ and $\theta_{1s}$, the results by DYMORE with a freewake model are quite good for all the test cases. However, the analysis with a finite-state dynamic inflow model under-predicts cyclic pitch angles.

From the above trim analyses results, although there are slight differences in the trimmed pitch control angles between the predictions and the test results, it is considered that the present modelings using finite-state dynamic inflow and freewake models can trim the HART II rotor successfully for the given flight conditions.

### *3.4 BVI airloads prediction*

When the relationship between BVI phenomena and rotor airloads is considered, BVI causes the fluctuations of rotor airloads with high frequency. These airloads oscillations can be seen definitely in the HART II test result [22]. Hence in BVI airloads calculation, it is important for numerical analysis to predict the number of and the locations of BVI events and the magnitude of airloads fluctuation by BVI. In this subsection, BVI airloads for three test cases of the HART II are predicted and the results are compared with the wind tunnel test results. In the present DYMORE analyses, two wake/inflow models such as free wake and finite-state dynamic inflow models are used. In addition, simply averaged test results are considered.

#### *3.4.1 Baseline (BL) case*

Fig. 7 shows the predicted and measured lifts, $M^2C_n$ at 87% span location for the BL case. The present results using the freewake model predict the 3/rev sectional lift variation quite reasonably although a phase shift is observed at 90 to 180 deg. rotor azimuth. It was one important issue in the HART I program to predict 3/rev lift related to vortex wake modeling capability. The measured data shows strong BVIs on the advancing (0 to 90 deg.) and retreating (270 to 360 deg.) sides. This is because the trailed tip vortices strike the blade again in the rotor plane, which results in significant BVI phenomenon. Although DYMORE with a freewake model misses the first two interactions on the advancing side, it shows good capability to predict lift oscillations with the high frequency due to BVIs. In the retreating region, the prediction with the freewake model captures both the number and the magnitude of BVIs nicely. However, DYMORE with a finite-state dynamic inflow model does not capture any BVI event since the induced inflow is assumed as simple harmonic functions. This result shows the importance of wake modeling in prediction of BVI airloads on the rotor blade in descending flight.

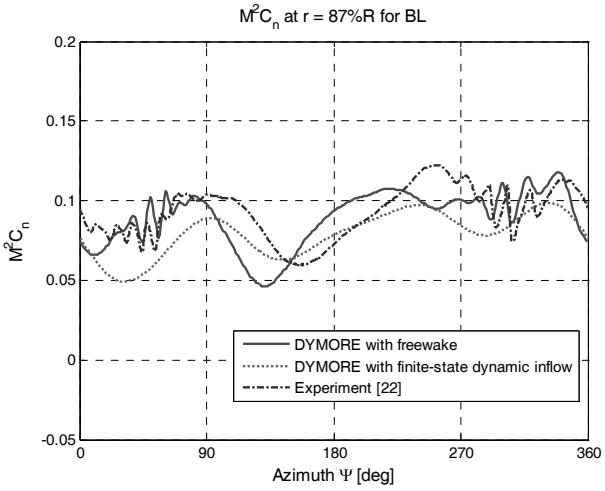


Fig. 7. Predicted and measured lifts at 87% span location for the BL case.

The alternative way to analyze BVI airloads is to investigate the gradient of the sectional lift with respect to the time or azimuth angle, $d(M^2C_n)/d\Psi$, since the highly impulsive and rapid fluctuating lifts during BVI induce sharp spikes in the sectional lift gradient. A larger magnitude of $M^2C_n$ gradient means a stronger BVI. The sectional lift gradients by DYMORE with a freewake model and the HART II wind tunnel test for the BL case are given in Fig. 8. Since DYMORE with a finite-state dynamic inflow model cannot capture the BVI well, as shown in Fig. 7 previously, its result is not considered in this example. The time step for DYMORE with a freewake model is 1 deg while the time step of the experimental data is 0.176 deg. Therefore, the results from DYMORE are interpolated by the spline interpolation method with a time step of 0.25 deg. The present $M^2C_n$ gradient at 87% span location for one rotor revolution is compared with the experimental result reasonably, as shown in Fig. 8(a). On the advancing side, as shown in Fig. 8(b), although the first two BVIs are missed and there is a slight phase shift, the present result shows a good correlation with the wind tunnel test result. In addition, the sectional lift gradient on the retreating side as given in Fig. 8(c) is predicted quite well although there is still a slight phase shift. However, the present prediction under-predicts the magnitude of BVI at the azimuth angle of around 305 deg. In Figs. 8(b) and (c), the peaks of BVIs in the advancing side are more than those in the retreating side. Furthermore, the BVIs in the advancing side are more impulsive.

Fig. 9 shows the predicted lift distribution with a freewake model on the rotor disk for the BL case. As seen in the figure, strong and a number of BVI peaks in the advancing and retreating regions on the rotor disk are noticed. Furthermore, the BVIs on the advancing side extend more inboard along the blade span as compared with BVIs on the retreating side.

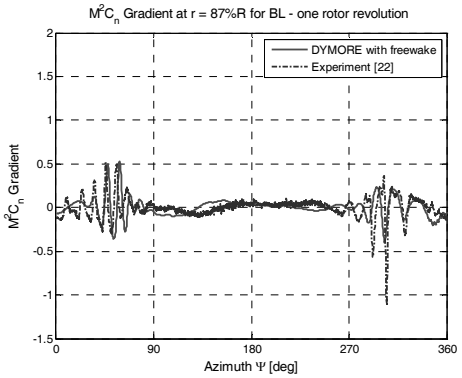


(a) Gradient of sectional lift for one rotor revolution

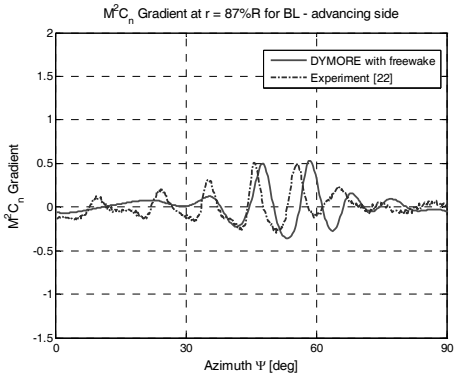


(b) Gradient of sectional lift in advancing side

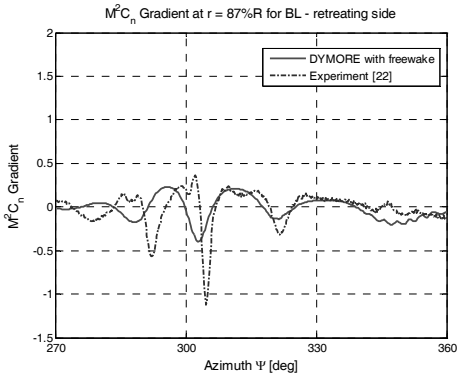


(c) Gradient of sectional lift in retreating side

Fig. 8. Predicted and measured sectional lift gradients at 87% span location for the BL case.

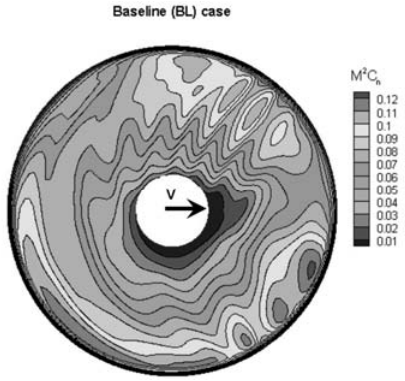


Fig. 9. Lift distributions on rotor disk for the BL case.

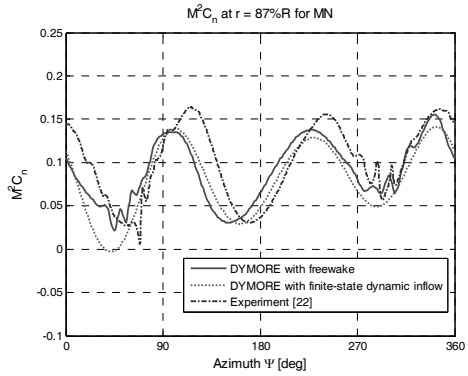


Fig. 10. Predicted and measured lifts at 87% span location for the MN case.

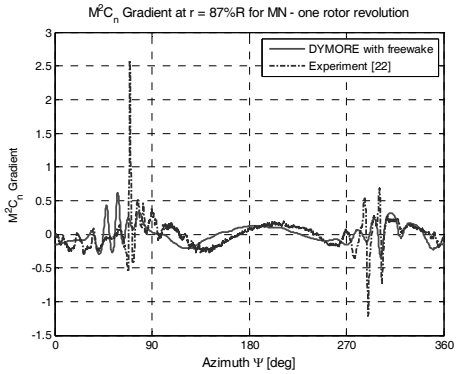


(a) Gradient of sectional lift for one rotor revolution

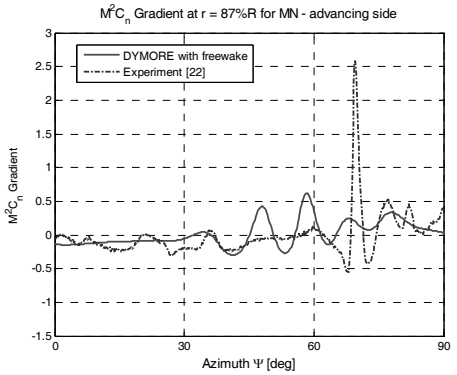


(b) Gradient of sectional lift in advancing side

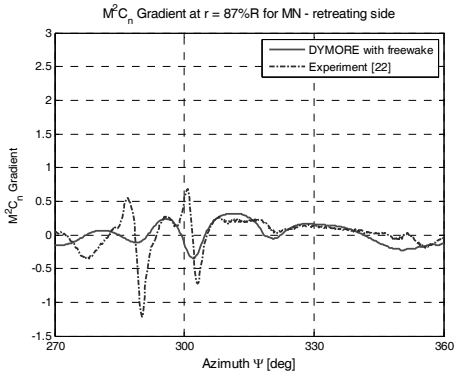


(c) Gradient of sectional lift in retreating side

Fig. 11. Predicted and measured sectional lift gradients at 87% span location for the MN case.

### *3.4.2 Minimum Noise (MN) case*

Following the correlation study of the previous BL case, the BVI airload for the MN case is predicted. Fig. 10 gives the predicted and measured lifts, $M^2C_n$, at 87% span location for the MN case. As compared with the BL case, 3/rev sectional lift variations in both the measured data and the prediction become stronger since 3/rev HHC inputs given in Table 2 are introduced for this MN case. It is noticeable that the number of measured BVI events is reduced significantly. It is indicated that the sectional lifts of the MN case are increased in the second quadrant in both the measurement and the present predictions, as compared to the BL case. In this region, the circulation of the trailed tip vortices could be larger so that the induced velocity becomes increased. This increased induced velocity along with the elastic flap motion will increase the miss-distance which is defined as the vertical distance between the rotor blade and the tip vortices and one of driving factors affecting BVI. In the end, the vortices may pass far away from the blade without causing significant BVI oscillations. The effect of blade flap motions on the miss-distance will be discussed in the later section. Furthermore there is a strong BVI in the test result at the azimuth angle of around 68.5 deg. due to the HHC control setting. The BVI airload prediction by DYMORE with a freewake model is relatively good on both advancing and retreating sides. However, a slight phase shift similar to that in the BL case is observed in the present predictions. DYMORE using a finite-state dynamic inflow model shows a similar trend of overall lift variation in both the prediction with a freewake model and the test results. However, the lift oscillations with the high frequency are not observed in both advancing and retreating sides.

The sectional lift gradient at 87% span location for the MN case is shown in Fig. 11. The number, magnitudes, and locations of predicted BVIs on the advancing side as seen in Fig. 11(b) are not as good as the prediction results for the BL case. On the retreating side, shown in Fig. 11(c), although the magnitudes of BVI spikes are somewhat lower and the pulse-widths are wider than those values in the wind tunnel test results, the trend of BVI phenomena is quite similar to that in the measured data.

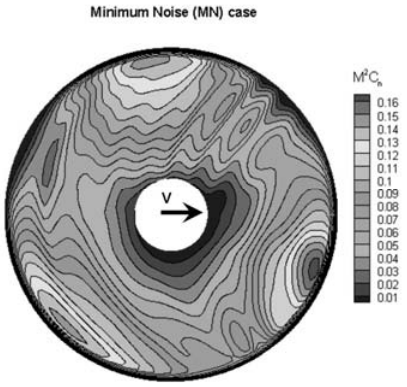


Fig. 12. Lift distributions on rotor disk for the MN case.

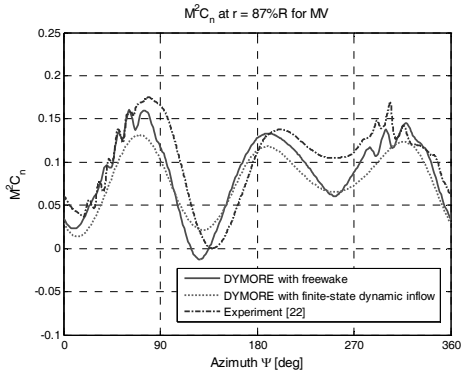


Fig. 13. Predicted and measured lifts at 87% span location for the MV case.

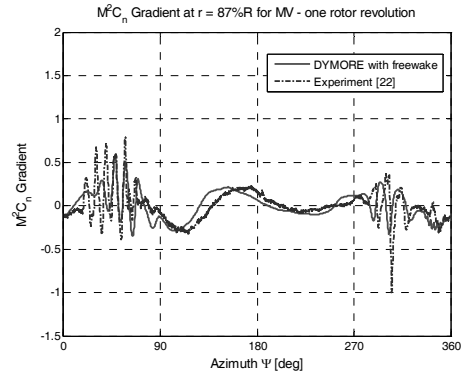


(a) Gradient of sectional lift for one rotor revolution

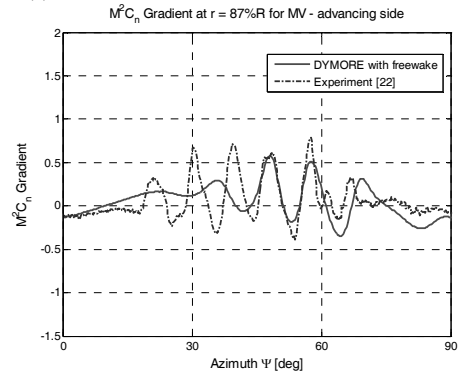


(b) Gradient of sectional lift in advancing side

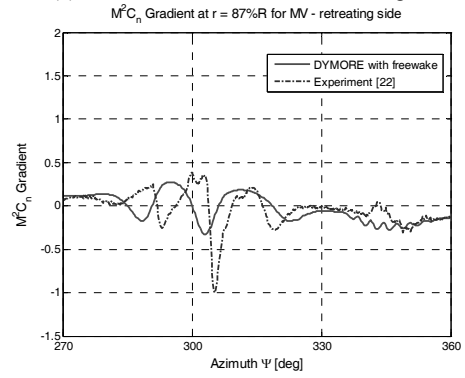


(c) Gradient of sectional lift in retreating side

Fig. 14. Predicted and measured sectional lift gradients at 87% span location for the MV case.

The predicted lift distribution with a freewake model for the MN case is given in Fig. 12. As compared with the BL case, it is indicated that the number of BVI peaks on the rotor disk is significantly reduced with the introduction of the 3/rev control inputs. Particularly, no BVI peaks are noticed at the blade tip on the advancing side, which is the main reason for reduced noise emission in the MN case.

### *3.4.3 Minimum Vibration (MV) case*

BVI airloads prediction at 87% span location for the MV case is investigated. Likewise, in the previous MN case, the measured and predicted lifts for the MV case in Fig. 13 show more distinct 3/rev lift variation as compared with the BL case, since the MV case also uses the 3/rev HHC inputs given in Table 2. Note that the cosine and sine components of HHC inputs for the MV case are different from those of the MN case. On the contrary to the previous MN case, the sectional lifts in the second quadrant become decreased to nearly zero, which reduces the induced velocity significantly. The decreased induced velocity with the blade flap motion leads to a reduction of the miss-distance, which produces multiple fluctuations of sectional airloads in the first quadrant of the disk. These BVIs may generate more noise, as compared with the BL case. For the MV case, therefore, the vibration is reduced but the noise is increased. Although the prediction with a freewake model still shows a slight phase shift and misses the first two BVIs in the first quadrant, BVI airload is captured well for one rotor revolution. However, the present analysis under-predicts the sectional lift magnitude at the azimuth angle of around 250 deg. The prediction using a finite-state dynamic inflow model shows a quite reasonable lift variation trend except that there are no BVI phenomena. For the MV case, the sectional lift gradient is investigated in Fig. 14. As one can see, DYMORE with a freewake model predicts BVI spikes nicely on both advancing and retreating sides. It is observed that the first two BVIs are missed, which is similar to the result in the BL case and the BVI magnitude at the azimuth angle of around 305 deg is under-predicted.

Fig. 15 depicts the lift distribution calculation with a freewake model on rotor disk for the MV case. Although the maximum and minimum of the lift are quite similar to those in the previous MN case, the number of and locations of BVIs for the MV case are different from those for the MN case. It is indicated that there is a negative lift around the blade tip on the advancing side that may produce a pair of vortices which are counter-rotating with each other and push up the vortices as observed in the HART II experiment [22].

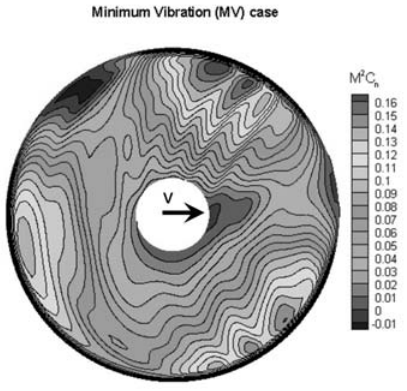


Fig. 15. Lift distributions on rotor disk for the MV case.

### *3.5 Blade deformations*

The elastic deformations at the blade tip such as flap bending, lead-lag bending, and torsion are discussed for the BL, MN, and MV cases. Especially the flap responses for the MN

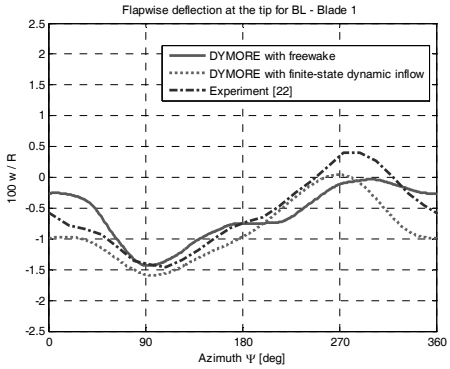


(a) Flap deflection

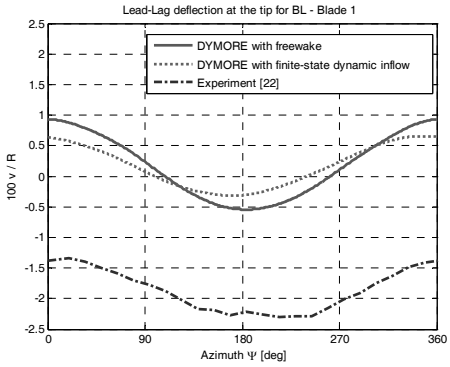


(b) Leadlag deflection

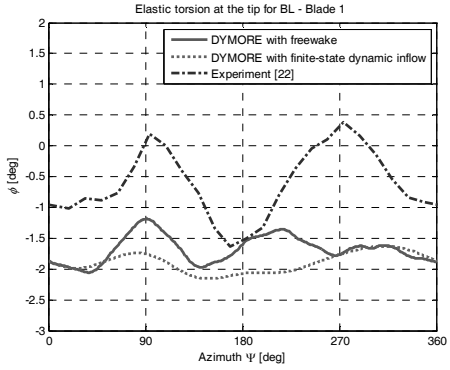


(c) Elastic torsion deformation

Fig. 16. Blade deformations at the tip for the BL case.

and MV cases are considered to investigate the miss-distance which is mentioned in the previous section. All predictions are compared with the measured data for the blade 1 which is defined in Fig. 5.

Fig. 16 shows the blade deformations at the tip for the BL case. For the flapwise deflection as given in Fig. 16(a), the present predictions with the two wake/inflow models show reasonable correlation with the measurement data. The lead-lag deflection results are seen to have a constant offset with the measured values by about one-third chord lengths as seen in Fig. 16(b). This offset has also observed in other HART II analysis [8]. However the predicted waveforms match well with the measured data. Fig. 16(c) presents the elastic torsion response. The peak-to-peak magnitudes of the predicted twist response are slightly lower than the measured data, but, overall, an acceptable correlation is obtained.

The blade tip responses for the MN case are shown in Fig. 17. As is seen, the present analyses with two different wake/inflow models predict the tip flap deflection reasonably well as compared with the test result. In this specific case, the prediction with a finite-state dynamic inflow model gives better correlation than that with a freewake model. As discussed in Section 3.4.2, the flap deflection at the blade tip is closely related to the miss-distance at two particular azimuth angles related to vortex generation and blade vortex interaction. As is presented in Fig. 17(a), the blade flaps down at the azimuth angle of around 130 deg. where a tip vortex is generated, while the blade flaps up at the azimuth angle of around

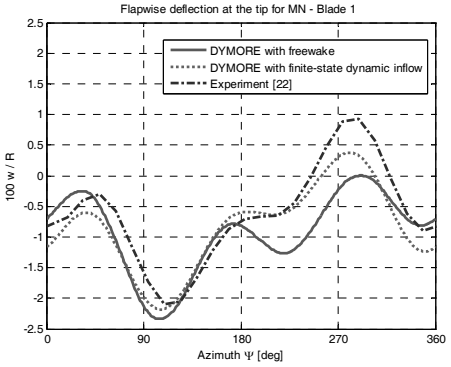


(a) Flap deflection

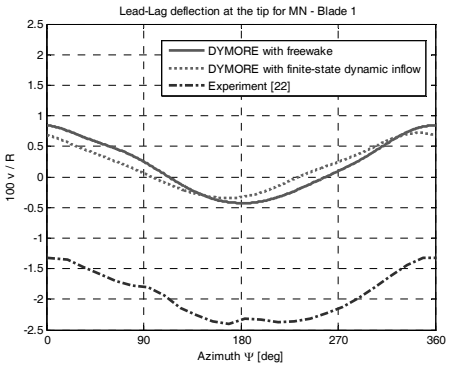


(b) Leadlag deflection

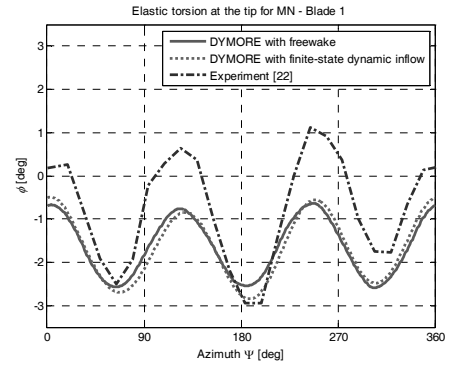


(c) Elastic torsion deformation

Fig. 17. Blade deformations at the tip for the MN case.

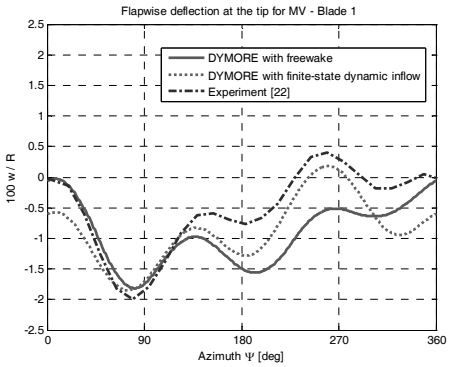


(a) Flap deflection

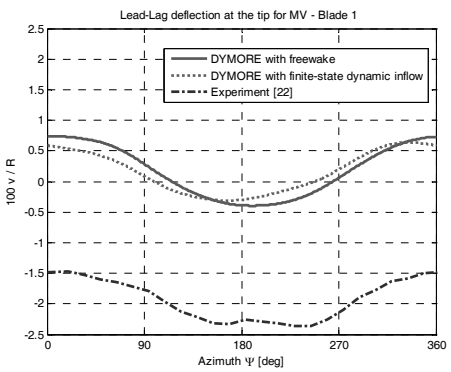


(b) Leadlag deflection

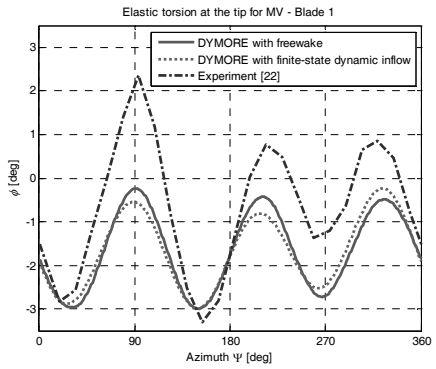


(c) Elastic torsion deformation

Fig. 18. Blade deformations at the tip for the MV case.

60 deg. where the interaction between the blade and the tip vortex is caused. This flap motion increases the miss-distance, which may reduce the rotor noise emission for the MN case. Fig. 17(b) gives the calculated lead-lag deflections at the tip. Similar to the BL case, the present predictions have a constant offset from the measurement. Fig. 17(c) shows the tip elastic torsion deformations in measurement and predictions. The elastic torsion deformation shows a clear 3/rev response due to the introduction of 3/rev harmonic inputs in the MN case. Except the constant offset in the lead-lag bending, a good agreement between the present predictions and the test data is obtained.

Fig. 18 shows the blade deformations at the tip for the MV case. The correlation shows quite a similar trend with the previous MN case for each of flap, lead-lag, and torsion deformations. However, the behavior of flap deflections at two specified locations for vortex generation and blade vortex interaction appear almost opposite to the previous MN case. It is seen that this reversed situation reduces the miss-distance for the MV case, which cause significant fluctuations of airloads on the advancing side.

## 4. Conclusions

The present work investigated the prediction capability of DYMORE with a free vortex wake model for a rotor in descending flight condition over the conventional finite-state dynamic inflow model. Based on the analytic study, the following conclusions were drawn.

1) The DYMORE analysis with a free wake model improved the evaluation of collective and cyclic pitch control settings as compared with the measured values.

2) Due to the introduction of free wake analysis, significant improvement of BVI airload predictions were achieved in both the advancing and retreating sides of the rotor disk. Many BVI peaks were captured with the free wake analysis, although some BVI peaks were missed and a slight phase shift was observed on the advancing side.

3) The mechanism of reducing noise or vibration levels in the MN or MV case was identified. For MN case, it was found that the blade flapped down at the azimuth of 130 deg. where a tip vortex was generated, while the blade flapped up at azimuth of 60 deg. where the interaction between the blade and the tip vortices was caused. The resulting flap motion increased the miss distance leading to a low noise emission for the MN case. Whereas in the MV case, the flap response at the two specified locations showed almost opposite behavior as compared with the MN case, which might cause significant airload fluctuations on the advancing side.

## Acknowledgment

This work was supported by the National Research Foundation through a grant provided by the Korean Ministry of Education, Science & Technology (MEST) in 2009 (No. K20601000001) and Defense Acquisition Program Administration and Agency for Defense Development under the contract UD070041AD. The first author expresses sincere thanks to Prof. Bauchau, Dr. Liu at Georgia Institute Technology, and Dr. Roget at National Institute of Aerospace (NIA) for their valuable help. The authors thank the HART II team for the test data.

## References

[1] Y.-H. Yu, B. Gmelin, H. Heller, J. J. Phillippe, E. Mercker and J. S. Preisser, HHC aeroacoustics rotor test at the DNW – The joint German/French/US HART project, *Proc. of 20th European Rotorcraft Forum*, Amsterdam, Netherlands, (1994).

[2] Y.-H. Yu, C. Tung, B. G. van der Wall, H.-J. Pausder, C. Burley, T. Brooks and P. Beaumier, Y. Delrieux, E. Mercker, K. Pengel, The HART-II test : rotor wakes aeroacoustics with Higher-Harmonic pitch Control (HHC) inputs -The joint German/French/Dutch/US project-, *Proc. of the American Helicopter Society 58th Annual Forum*, Montreal, Canada, (2002).

[3] J. Bailly, Y. Delrieux and P. Beaumier, HART II: Experimental analysis and validation of ONERA methodology for the prediction of blade-vortex interaction, *Proc. of 30th European Rotorcraft Forum*, Marseilles, France, (2004).

[4] J.-W. Lim and B. G. van der Wall, Investigation of the effect of a multiple trailer wake model for descending flights, *Proc. of the American Helicopter Society 61st Annual Forum*, Grapevine, Texas, USA, (2005).

[5] H.-S. Yeo and W. Johnson, Assessment of comprehensive analysis calculation of airloads on helicopter rotors, *Journal of Aircraft* 42(5) (2005) 1218-1228.

[6] J.-W. Lim, T. A. Nygaard, R. Strawn and M. Potsdam, BVI airloads prediction using CFD/CSD loose coupling, *Proc. of the American Helicopter Society 4th Vertical Lift Aircraft Design Conference*, San Francisco, CA, USA, (2006).

[7] M. J. Hill, *Coupled fluid-structure simulations of helicopter* rotors, *MS thesis*, *The Pennsylvania State University*, University Park, PA, USA, (2006).

[8] J.-W. Lim, An assessment of rotor dynamics correlation for descending flight using CSD/CFD coupled analysis, *Proc. of the American Helicopter Society 64th Annual Forum*, Montreal, Canada, (2008).

[9] B.-Y. Min, L. N. Sankar and Y.-H. Yu, Recent improvements to the hybrid methodology for modeling HART-II BVI phenomena, *6th HART II International Workshop*, Riverpool, UK, (2008).

[10] S.-J. Shin, *Integral twist actuation of helicopter rotor blades for vibration reduction*, *Ph.D thesis, Massachusetts Institute of Technology*, Cambridge, MA, USA, (2001).

[11] B. Roget, Simulation of active twist and active flap control on a model-scale helicopter rotor, *Proc. of 24th Applied Aerodynamics Conference*, San Francisco, CA, USA, (2006).

[12] J. Shen, P. Masarati, B. Roget, D. J. Piatak, M. W. Nixon

and J. D. Singleton, Stiff-inplane tiltrotor aeromechanics investigation using two multibody analyses, *Proc. of Multibody dynamics*, Milano, Italy, (2007).

[13] J.-S. Park and S.-J. Shin, Vibratory loads reduction analysis of advanced active twist rotor blades incorporating single crystal piezoelectric fiber composites, *Proc. of the American Helicopter Society Specialists' Conference on Aeromechanics*, San Francisco, CA, USA, (2008).

[14] O. A. Bauchau, Computational Schemes for Flexible, *Nonlinear Multi-Body Systems Multibody System Dynamics* 2 (1998) 169-225.

[15] D. H. Hodges, A mixed variational formulation based on exact intrinsic equations for dynamics of moving beams, *International Journal of Solids and Structures*, 26 (1990) 1253-1273.

[16] D. A. Peters and C. J. He, Finite State Induced Flow Models Part II: Three-Dimensional Rotor Disk, *Journal of Aircraft* 32(2) (1995) 323-333.

[17] H. Liu, Interfacing comprehensive rotorcraft analysis with advanced aeromechanics and vortex wake models, Ph.D thesis, Georgia Institute of Technology, Atlanta, GA, USA, (2008).

[18] M. J. Bhagwat, J. G. Leishman, Stability, consistency and convergence of time-marching free-vortex rotor wake algorithms, *Journal of the American Helicopter Society* 46 (2001) 59-71.

[19] V. Milenkovi, Coordinate suitable for angular motion synthesis in rotors, *Proc. of the Robot VI Conference*, Detroit, MI, USA, (1982).

[20] B. G. van der Wall, *2nd HHC Aeroacoustic Rotor Test (HART II) - Part I: Test documentation-, Institute Report IB 111-2003/31, German Aerospace Center (DLR)*, Braunschweig, Germany, (2003).

[21] P. Wierach, S. Opitz and J. Riemenschneider, Status of DLR Active Twist Blade, *1st HART III Preparatory Meeting*, Montreal, Canada, (2008).

[22] B. G. van der Wall, 2nd HHC Aeroacoustic Rotor Test (HART II) - Part II: Representation results-, Institute Report IB 111-2005/03, German Aerospace Center (DLR), Braunschweig, Germany, (2005).

**Jae-Sang Park** received Ph.D degree in mechanical and aerospace engineering, from Seoul National University, Seoul, Korea in 2006. From 2006-2007, he worked as a post doctor at Flight Vehicle Research Center, Seoul National University. Dr. Park is currently a research professor at Konkuk University, Seoul, Korea. His research interests include aeroelasticity, rotorcraft aeromechanics using multibody dynamics, and smart structures.

**Sung Nam Jung** is a professor at the Department of Aerospace Information Engineering in Konkuk University, Seoul, Korea. He received his PhD, MS, and BS degrees from Seoul National University, Seoul, Korea in 1993, 1989, and 1986, respectively. He visited the University of Maryland, College Park in USA as a visiting assistant professor in 1999 and as an adjunct professor at Kaist in 2005. From 1994 to 2006, he worked for Chonbuk National University as a faculty member. He joined the Konkuk University as a full professor in 2006. The areas of interests include rotorcraft dynamics, aeroelasticity, composite structural mechanics, and smart structures and materials.